

Influence of pressure guidewire on coronary hemodynamics and fractional flow reserve

Xuanyu Li (李璇宇),^{1,2,3} Zhi Zhang (张治),⁴ Sergey Simakov,^{5,6} Timur Gamilov,^{6,7} Yuri Vassilevski,^{6,7} Yue Wang (汪月),⁸ and Fuyou Liang (梁夫友)^{1,2,3,7, a)}

¹⁾Department of Engineering Mechanics, School of Ocean and Civil Engineering, Shanghai Jiao Tong University, Shanghai 200240, China.

²⁾Key Laboratory of Hydrodynamics (MOE), School of Ocean and Civil Engineering, Shanghai Jiao Tong University, Shanghai 200240, China.

³⁾State Key Laboratory of Ocean Engineering, Shanghai Jiao Tong University, Shanghai 200240, China.

⁴⁾Department of Cardiology, Shanghai General Hospital, Shanghai Jiao Tong University School of Medicine, Shanghai 200080, China.

⁵⁾Moscow Institute of Physics and Technology, Dologoprudny 141701, Russia.

⁶⁾Marchuk Institute of Numerical Mathematics of the Russian Academy of Sciences, Moscow 119333, Russia.

⁷⁾Institute for Computer Science and Mathematical Modeling, Sechenov First Moscow State Medical University, Moscow 119991, Russia.

⁸⁾Department of Cardiology, Shanghai Ninth People's Hospital, Shanghai Jiao Tong University School of Medicine, Shanghai 200011, China.

Invasive measurement of coronary fractional flow reserve (FFR) routinely involves the use of a pressure guidewire that will induce hemodynamic changes, thereby causing the measured FFR to deviate from the intact in-vivo one. On the other hand, computational models used for predicting FFR often ignore the encroachment of vascular lumen by guidewire, which may compromise the comparability of model predictions with in-vivo measurements. In this study, a geometrical multiscale model was developed to quantify the influences of two types of pressure guidewire (i.e., pressure wire and pressure catheter) on coronary hemodynamics and FFR. Numerical experiments were conducted on thirty-five idealized and ten realistic models of the left anterior descending artery (LAD). Obtained results revealed that inserting a pressure guidewire into the LAD augmented the viscous pressure loss across the stenosis segment, leading to a decrease in blood flow rate, increase in trans-stenosis pressure drop, and consequently decrease in FFR. The guidewire-induced decrease in FFR was affected mainly by vascular diameter, stenosis rate, the number of stenosis, and the diameter of guidewire. More importantly, the study demonstrated the existence of a linear relationship between guidewire-present FFRs and guidewire-absent (intact) FFRs despite the large variations in stenosis rate and vascular morpho-geometrical characteristics, which could be explained by a theoretical model. These findings may serve as theoretical references for explaining or correcting the discrepancies between FFRs predicted by guidewire-absent models and in-vivo measurements or converting invasively measured FFRs into the intact ones to better assess the functional impact of coronary artery stenoses.

I. INTRODUCTION

Coronary artery disease (CAD), featured mainly by the presence of atherosclerotic stenosis or occlusion in epicardial coronary arteries, can lead to myocardial ischemia or even infarction, and is one of the major causes of cardiovascular death worldwide¹. In clinical practice, understanding the functional impairment of a coronary artery with stenosis is key to determining whether revascularization operation should be offered². In this context, coronary fractional flow reserve (FFR) was proposed to assess the functional severity of coronary artery stenosis^{3,4}, and has now become an important indicator for clinical decision-making². By definition, FFR is the ratio of the maximal blood flow rate in a stenosed coronary artery to the theoretical normal maximal flow rate in the stenosis-free state, whereas in clinical settings it is usually evaluated by means of calculating the ratio of the mean post-

stenosis pressure to the aortic pressure under a drug-induced hyperemic condition⁴.

The gold standard for measuring FFR generally involves the use of a guidewire (e.g., pressure wire (PW) or pressure catheter (PC)) to measure intravascular blood pressures. The procedure is however invasive, time-consuming, and expensive⁵. As an alternative means for overcoming the shortcomings of invasive FFR measurement, image-based computational fluid dynamics (CFD) methods have been proposed and widely applied in recent ten years⁶⁻⁹. Many studies have demonstrated the acceptable accuracy and clinical significance of model-predicted FFRs in comparison with the invasively measured counterparts^{10,11}. However, most model-based studies did not consider the presence of a pressure guidewire in the coronary artery that is deemed to be used in invasive FFR measurement. Physically, a pressure guidewire placed across a coronary artery stenosis will partly occupy the lumen space, thereby altering blood flow patterns and FFR in the coronary artery. Some researchers have carried out studies to address the hemodynamic impacts of pressure guidewire. Existing studies in this field were diverse with respect to the

^{a)}Author to whom correspondence should be addressed: fuyou-liang@sjtu.edu.cn

employed methods and research objectives, including in-vitro experiments^{12,13} and numerical simulations conducted on idealized coronary artery geometries^{14–16} as well as numerical studies based on patient-specific data^{17,18}. Common findings from these studies include: 1) pressure guidewire augments the trans-stenosis pressure drop, leading to an underestimation of FFR, and 2) the hemodynamic effects of pressure guidewire become more pronounced as the severity of stenosis increases. In addition, some studies revealed that guidewire-induced changes in FFR were sensitive to coronary blood flow rate^{18,19}. The majority of these studies are however subjected to limitations. For instance, the same inflow rate/waveform was often set in in-vitro experiments or assigned to computational models before and after guidewire insertion, which essentially ignored the pressure guidewire-induced change in flow rate that is deemed to occur under in-vivo conditions and therefore might cause the obtained results unable to fully characterize the real physiological phenomena. Moreover, no studies systematically investigated how the influence of pressure guidewire on FFR is affected by the morpho-geometrical characteristics of coronary artery and stenosis that usually vary considerably from one patient to another. In addition, few studies explored in detail the fluid dynamics mechanisms underlying the observed changes in trans-stenosis pressure drop and FFR following the insertion of a pressure guidewire.

To address the aforementioned issues, we developed a geometrical multiscale modeling method, which is featured by the integration of a three-dimensional (3D) model of the left anterior descending artery (LAD) into a lumped-parameter (0D) model of the coronary circulation coupled to the cardiovascular system. In the multiscale model, the boundary conditions of the 3D model are automatically generated via the coupled solution of the 0D and 3D models, and hence can spontaneously change in response to the insertion of a pressure guidewire into the LAD or variations in the stenosis severity or morpho-geometrical characteristics of the LAD. With these features, the multiscale model provided a flexible tool for simulating the pressure guidewire-induced hemodynamic changes in any LADs of interest under physiologically reasonable conditions. A series of idealized 3D LAD models having different morpho-geometrical features and containing stenoses of various severities were created. In addition, ten realistic LAD models were reconstructed based on medical images. Each LAD model was embedded in the multiscale model to simulate the blood flow rates, trans-stenosis pressure drops, and FFRs before and after the insertion of a pressure guidewire (PW or PC). Furthermore, the obtained numerical results for all the models were collectively analyzed to elucidate the general fluid dynamics mechanisms underlying the increase in trans-stenosis pressure drop following the insertion of a pressure guidewire, identify factors that augment guidewire-induced FFR changes, as well as explore the relationship between intact (guidewire-absent) FFRs and guidewire-present FFRs.

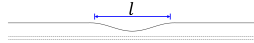
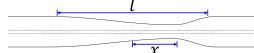
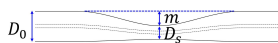
II. METHODS

A. Creation of geometric and mesh models

We generated thirty-five idealized LAD models that have different morpho-geometrical characteristics and contain one or multiple stenoses of various severities. The baseline morphology of stenosis was adopted from a previous study²⁰, and the major morpho-geometrical parameters being varied to create the models are summarized in TABLE I. Specifically, one set of models were designed to have varying stenosis rates (from 35% to 75%), whereas the stenosis rate in the other models representing the morpho-geometrical variations of LAD, the morphological variations of stenosis, or the presence of multiple serial stenoses was fixed at 55% to represent moderate stenosis for which assessing FFR is of high clinical significance²¹. In addition, the geometric models of 10 realistic LADs having a moderate stenosis (stenosis rate = 50–60%) in the proximal portion were reconstructed based on computed tomography angiography (CTA) images using Mimics 16 (Materialise, Belgium). The reconstructed models were each read into SOLIDWORKS (Dassault Systèmes, France) where a vascular straightening treatment was performed to remove vascular curvature while maintaining the vascular cross-sectional shape and lumen area unchanged. This treatment was aimed to yield two sets of models (with and without vascular curvature, respectively) for investigating whether vascular curvature would affect the sensitivity of FFR to pressure guidewire insertion. A PW (PressureWire X, Abbott, USA) or PC (TRUEPHYSIO, Insight Lifetech, China) routinely used to measure intra-vascular blood pressure in the clinical practice was inserted in each LAD model along the vascular centerline (from the inlet to 40 mm downstream of the stenosis)²². The PW and PC had a diameter of 0.36mm and 0.53mm, respectively.

Each geometric model with or without an inserted pressure guidewire was read into ICEM (Ansys Inc., USA) to generate a mesh model. Herein, unstructured tetrahedral meshes were firstly created, with the meshes in the stenosis region or near the outer surface of guidewire being refined (see the locally highlighted mesh model in FIG. 1). Subsequently, five layers of prism elements were created from the vessel wall and guidewire outer surface toward the fluid domain. To ensure that the computed results are independent of element size, mesh sensitivity analysis was conducted on a randomly selected model. The results showed that the relative change in trans-stenosis pressure drop decreased below 0.05% when the global maximum size of tetrahedral elements was reduced from 0.2mm to 0.15 mm (see FIG. 2 (a)). Accordingly, a global maximum size of 0.15 mm was applied to all the models. It is noted that the maximum layer thickness of the prism elements was set to be smaller than the sizes of adjacent tetrahedral elements. The resulting mesh models contained varying numbers of elements, ranging from about 5 million to 7 million, with the specific element number of each mesh model determined by the complexity and size of the geometric model.

TABLE I. Definition of morpho-geometrical parameters and the ranges of their variations adopted for creating idealized LAD models. Morpho-geometrical parameters of the baseline model are: diameter=3.6 mm, curvature=0, tapering=1, number of stenosis=1, stenosis rate=55%, total vascular length=120mm, stenosis length=20mm, axial eccentricity=0, and radial eccentricity=0.

Morpho-geometrical parameters	Vascular/stenosis geometry	Definition	Range of variation
Diameter (mm)		D_0	2.6, 3.1, 3.6, 4.1, 4.6
Curvature (°)		$\cos^{-1}(\vec{n}_{in} \cdot \vec{n}_{out})$	0, 45, 90, 135, 180
Tapering		D_{in}/D_{out}	1, 1.25, 1.5, 1.75, 2
Number of stenosis		n	1, 2, 3, 4, 5
Stenosis rate (%)		$(1 - D_s/D_0) \times 100$	35, 45, 55, 65, 75
Stenosis length (mm)		l	5, 10, 20, 30, 40
Axial eccentricity (%)		$2x/l \times 100$	-75, -50, -25, 0, 25, 50, 75
Radial eccentricity (%)		$(\frac{2m}{D_0 - D_s} - 1) \times 100$	0, 25, 50, 75, 100

B. Development of a geometrical multiscale model

A geometrical multiscale modeling method²³ was employed to integrate each 3D LAD model into a lumped-parameter (0D) model of the coronary circulation coupled to the global cardiovascular system (see FIG. 1). The 0D model was adapted with simplifications from the models developed in previous studies^{24,25}, only including the major components of the cardiovascular system (i.e., the heart, pulmonary circulation and systemic circulation) and coronary circulation (i.e., large epicardial arteries and intramyocardial vessels allocated in three myocardial layers), nevertheless, it was sufficient to provide physiologically reasonable boundary conditions for the 3D LAD model. Coupling of the 0D and 3D models allowed the resulting multiscale model to automatically account for the changes in blood flow and FFR in the LAD upon the insertion of a pressure guidewire.

The parameters in the 0D model were initially assigned based on the data reported in a previous study²⁴ to represent the population-averaged cardiovascular properties. The resistances (R), compliances (C) and inductances (L) of epicardial coronary arteries and intramyocardial vessels in the 0D model of the coronary circulation were estimated by integrating the parameter values in a detailed coronary circulation model²⁶. To enable the model to simulate the hyperemic condition under which FFR is measured, some model parameters (e.g., heart rate, ventricular elastance, intramyocardial vascular resistance, and systemic vascular resistance) were further tuned

TABLE II. Comparison of model simulations and in-vivo measurements^{27,28} under the hyperemic condition. The in-vivo data are presented in form of mean \pm SD (standard deviation).

Parameters ^a	In vivo measurement	Simulation
HR (beats/min)	96.0 \pm 11.0	96.0
CO (L/min)	7.60 \pm 1.19	7.60
SBP (mmHg)	113.0 \pm 6.0	113.50
DSB (mmHg)	70.0 \pm 5.0	69.70
Q_{LAD} (mL/min)	256.15 \pm 110.84	256.20
Q_{LCX} (mL/min)	163.85 \pm 67.18	164.60
Q_{RCA} (mL/min)	217.69 \pm 76.70	216.40

^a Abbreviations: HR, heart rate; CO, cardiac output; SBP, systolic blood pressure; DBP, diastolic blood pressure; Q , time-averaged blood flow rate; LAD, left anterior descending artery; LCX, left circumflex artery; RCA, right coronary artery.

so that the model-simulated hemodynamic quantities (e.g., arterial blood pressure, flow rates in larger coronary arteries) fall in the ranges of in-vivo data^{27,28} (see TABLE II). The details of the assigned model parameter values are provided in TABLE III in the Appendix.

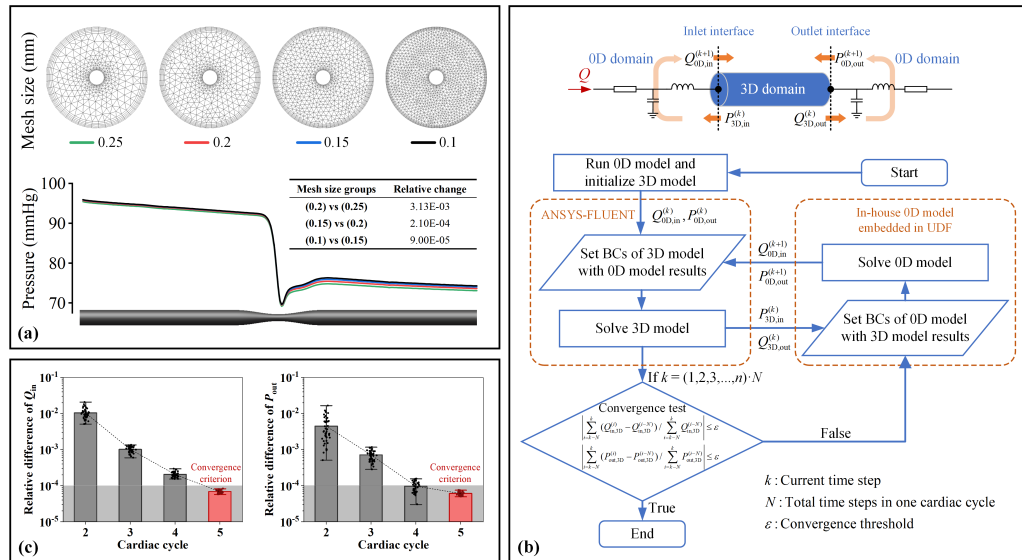


FIG. 2. Relative changes in computed trans-stenosis pressure drop when the global maximum size of tetrahedral elements is reduced from 0.25mm to 0.1mm in a stepwise manner (a), flowchart of the coupled solution of the 0D and 3D models (b), relative differences of the 0-3D model-computed flow rates (Q_{in}) and pressures (P_{out}) in two consecutive cardiac cycles (herein termed as convergence indicators) at the inlets and outlets of the forty-five LAD models (including thirty-five idealized models and ten realistic models) involved in the study (c). In panel (c), the scatter points represent the convergence indicators corresponding to individual LAD models with their statistical distributions being indicated by the error bars, while the histograms show the mean values of the convergence indicators of all the LAD models.

pressure wire were measured³¹. Herein, the $k-\omega$ turbulence model, which has been proved to be suitable for computing blood flows in stenosed vessels³², was employed. It is noted that only the mean pressures (i.e., time-averaged values of transient pressures over a cardiac cycle) are compared, although both the numerical and experimental studies were conducted under pulsatile flow conditions. The results showed that in comparison with the laminar model, the $k-\omega$ turbulence model provided a more accurate prediction of the measured pressure variations along the vessel with or without an inserted pressure wire, especially in the flow recirculation zone downstream of the stenosis (see FIG. 3). The advantage of the turbulence model became more evident following the increase in flow rate. Therefore, the $k-\omega$ turbulence model was employed to compute the blood flows in all the 3D LAD models involved in the present study, and accordingly the governing equations were expressed in form of the Reynolds-averaged Navier Stokes (RANS) equations.

2. Numerical methods and implementation of 0D-3D model coupling

The governing equations of the 0D model expressed in form of ordinary differential equations were solved with the explicit

fourth-order Runge-Kutta method, while the RANS equations of the 3D model were discretized and numerically solved with second-order schemes for both the temporal and spatial terms using a well-validated CFD package FLUENT (ANSYS Inc., USA). The key point herein is the coupled solution of the two models in a time-marching manner. In this study, we exchanged hemodynamic quantities between the two models by imposing mass and momentum conservation conditions at the 0D-3D model interfaces (located at the inlet and outlet of the 3D model). FIG. 2 (b) shows the procedure of coupled numerical solution for the 0D and 3D models. The procedure includes the following steps: 1) the 0D model incorporated with the estimated viscous and Bernoulli's resistances of the 3D model is firstly run for tens of cardiac cycles to achieve a periodic solution, which provides hemodynamic quantities at the k th time step ($t = k\Delta t$) for prescribing the boundary conditions of the 3D model at the 0-3D model interfaces, i.e., volumetric flow rate at the inlet interface ($Q_{0D,in}^{(k)}$) and the pressure at the outlet interface ($P_{0D,out}^{(k)}$); 2) the 3D model computes the flow velocities and pressures in the 3D domain using an implicit scheme, and feeds the updated mean pressure at the inlet interface ($P_{3D,in}^{(k)}$) and flow rate at the outlet interface ($Q_{3D,out}^{(k)}$) back to the 0D model; and 3) with the pressure and flow rate received from the 3D model used as the boundary conditions,

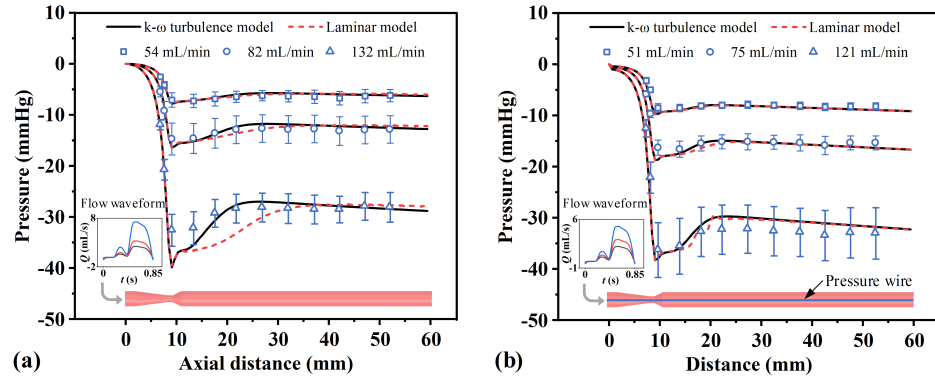


FIG. 3. Comparisons between the computed and experimentally measured variations of pressure (relative to the inlet pressure) along a stenosed vessel without (a) or with (b) an inserted pressure wire under various flow rate conditions. The numerical simulations and experiments were both conducted under pulsatile flow conditions, as characterized by the illustrated inlet flow waveforms and the corresponding mean flow rates. The plotted pressure data are the mean values of the computed/measured transient pressures over a cardiac cycle. The computations are carried out using a laminar model and a $k-\omega$ turbulence model, respectively.

the 0D model computes the flow rate and pressure at the interfaces ($(Q_{0D,in}^{(k+1)})$, $(P_{0D,out}^{(k+1)})$) for the next (i.e., $(k+1)$ th) time step with an explicit numerical scheme, which are again used to prescribe the 3D model boundary conditions at the $(k+1)$ th time step. The data exchanges between the 0D and 3D models proceed over time for several cardiac cycles until the relative differences between the computed hemodynamic quantities (herein, the inlet flow waveform and outlet pressure waveform of the 3D model) in two consecutive cardiac cycles both reach a value lower than the threshold of convergence ($\epsilon < 0.0001$). FIG. 2 (c) shows that the numerical coupling procedure converged within five cardiac cycles for all the LAD models involved in the study. The computed hemodynamic data in the last cardiac cycle were extracted for further analysis.

The computer code for solving the 0D model was programmed with the C language, and was embedded into FLUENT via User Defined Functions (UDF) to facilitate data exchanges between the 0D and 3D models. The numerical time steps (Δt) of the 0D and 3D models were set to be the same, with a fixed value of 0.001s. Each set of numerical simulation was conducted on a workstation equipped with an AMD EPYC 7542 32-Core Processor and 256 GB DDR RAM, and took approximately 8 hours to obtain converged solutions.

D. Analysis of trans-stenosis pressure drop

For each LAD model, the computed trans-stenosis pressure drop (ΔP) was further decomposed into three components in light of a classical theoretical stenosis model established based on in-vitro experimental data^{33,34}. This data processing was aimed to facilitate the analysis of hemodynamic mechanisms

behind the changes in ΔP following the insertion of a pressure guidewire.

$$\Delta P = \Delta P_R + \Delta P_B + \Delta P_L, \quad (1)$$

where

$$\Delta P_R = R \times Q, \quad \Delta P_B = B \times Q|Q|, \quad \Delta P_L = L \times \frac{dQ}{dt}. \quad (2)$$

Here, ΔP_R represents the viscous pressure loss along the vascular axis, ΔP_B accounts for the energy dissipation caused by flow recirculation or turbulence that usually occurs in regions with sudden lumen area changes, such as the post-stenosis region, and ΔP_L reflects the inertial effects of blood flow. The three coefficients (R , B , and L) in Eq.(2) are generally termed as viscous resistance, Bernoulli's resistance, and inductance, respectively.

In a stenosed vessel with complex anatomical structure, R , B , and L are affected by multiple morpho-geometrical parameters and are sensitive to hemodynamic conditions, making it difficult to define exact theoretical formulas for them. In this regard, we performed multivariable regression analysis based on the computed relationship between trans-stenosis pressure drop and flow rate in each individual LAD model during a cardiac cycle, thereby numerically deriving the values of R , B , and L and the corresponding components of trans-stenosis pressure drop. FIG. 4 (a) shows the results of regression data analysis for a LAD model in three states (i.e., absence of pressure guidewire, presence of a PW, and presence of a PC). It is clear that with the derived values of R , B , and L , Eqs. (1) and (2) can accurately fit the model-simulated relationship between trans-stenosis pressure drop and flow rate ($r^2 > 0.99$).

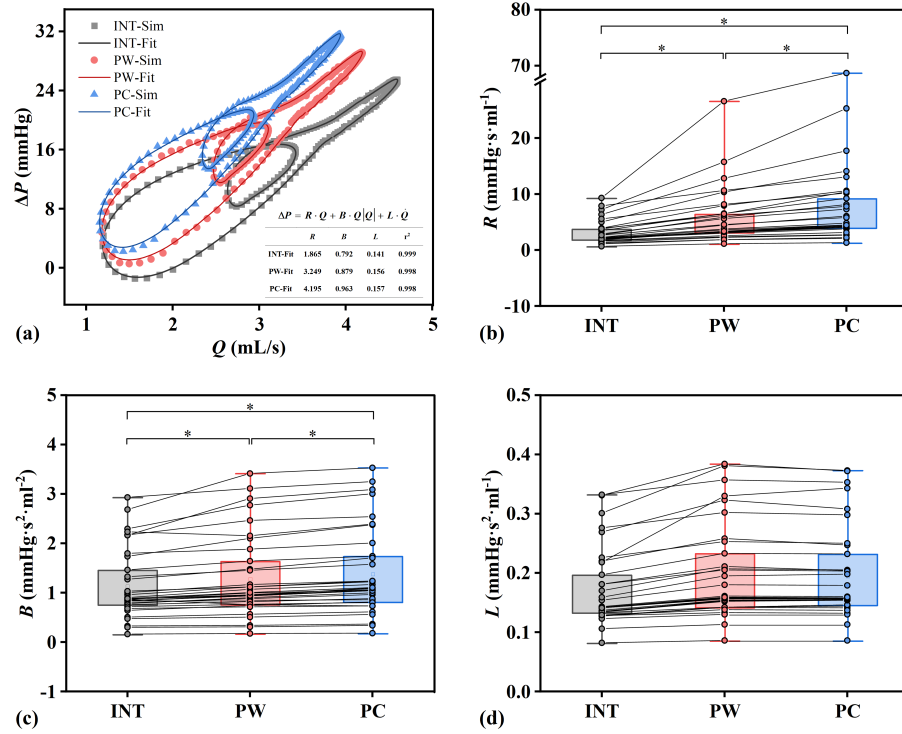


FIG. 4. Estimation of R , B and L in the theoretical model of trans-stenosis pressure drop (ΔP) via multivariable regression analysis of the 3D model-computed ΔP -flow rate (Q) relationship in a LAD model without or with an inserted pressure guidewire (a), box plots of the estimated R (b), B (c), L (d) for all the forty-five LAD models without or with an inserted pressure guidewire. The scattered points represent individual data values, while the colored rectangles represent the lower and upper quartiles of each dataset with the error bars indicating the minimum and maximum values. All the inter-group comparisons are performed with paired t-test, with the stars (*) indicating a p value of <0.001 . Abbreviations: INT, intact condition (absence of a pressure guidewire); PW, presence of a pressure wire; PC, presence of a pressure catheter.

III. RESULTS

A. Influence of pressure guidewire on coronary blood flow and trans-stenosis pressure drop

FIG. 5 shows the computed results for a series of LAD models with the same diameter while varying degree of stenosis before and after the insertion of a PW or PC. The flow waveform at the inlet (Q_{in}) and pressure waveform at the outlet (Q_{out}) of the LAD model changed automatically in response to the variations in stenosis rate or the insertion of a PW or PC (FIGs. 5 (a) & (b)). Following the increase in stenosis rate or the insertion of a PW or PC, the mean value of Q_{in} (averaged over a cardiac cycle) decreased, while the mean trans-stenosis

pressure drop (ΔP) increased (FIGs. 5 (c) & (d)). In comparison with the PW, the PC induced a greater decrease in Q_{in} and increase in ΔP due to the larger occupation of the lumen space. These results demonstrate the capability of the 0-3D multiscale model in simulating physiological hemodynamic responses to the alterations in LAD stenosis or the introduction of a pressure guidewire.

The computed trans-stenosis pressure drops for all the LAD models (including thirty-five idealized models and ten realistic models) with or without the insertion of a PW or PC were each decomposed into three components (i.e., ΔP_R , ΔP_B , and ΔP_L) along with the derived values of R , B , and L with the methods described in 'Section 2.4'. Paired t-test on the values of R , B , and L under the pressure guidewire-absent (i.e., intact), PW-inserted, and PC-inserted conditions indicated that

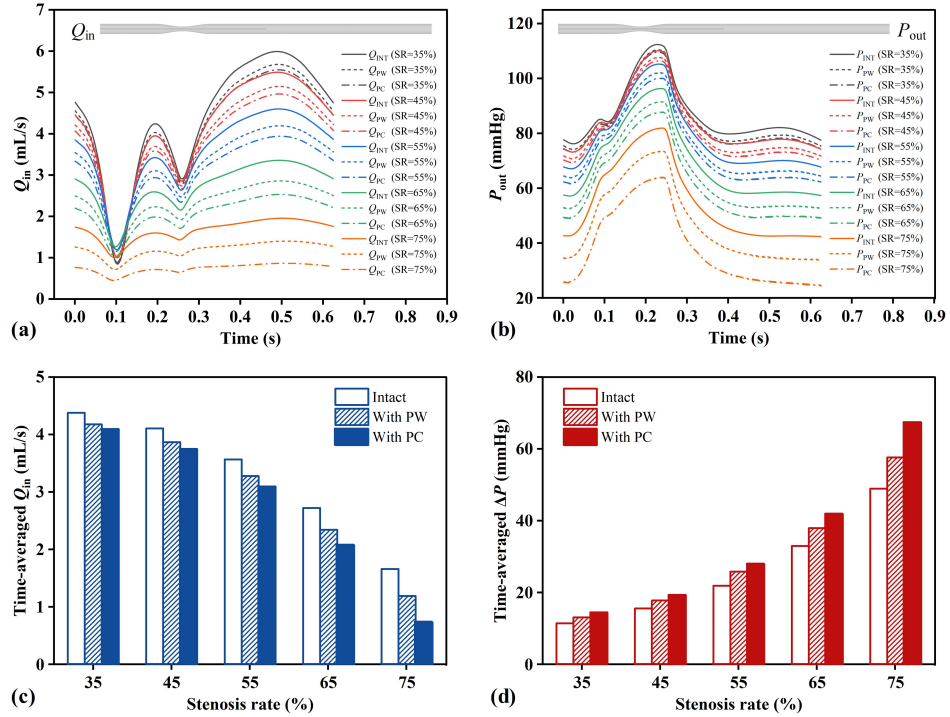


FIG. 5. 0-3D model-simulated flow waveforms at the inlets (Q_{in}) (a) and pressure waveforms at the outlets (P_{out}) (b) of LAD models with varying stenosis rate (SR) in the absence or presence of a pressure guidewire (PW or PC). Panels (c) and (d) display respectively the changes in mean inlet flow rate and trans-stenosis pressure drop (ΔP) (averaged over a cardiac cycle) following the increase in SR or the insertion of a PW or PC.

the insertion of a pressure guidewire significantly increased R , mildly enlarged B , while had statistically nonsignificant influence on L (FIGs. 4 (b-d)). The PC induced a larger increase in R than did the PW due to its larger diameter. Further comparing ΔP_R and ΔP_B (averaged over a cardiac cycle) under the three conditions revealed that ΔP_R was significantly elevated, whereas ΔP_B was slightly reduced despite the increase in B following the insertion of a PW or PC (see FIGs. 6 (a) & (b)). The decrease in ΔP_B after the insertion of a pressure guidewire is caused mainly by the reduced flow rate (see FIG. 5). The pressure guidewire-induced differential changes in ΔP_R and ΔP_B can be more clearly manifested if their relative contributions (quantified by percent proportion) to the total trans-stenosis pressure drop (ΔP) are compared (FIGs. 6 (d) & (e)). In all the samples, the statistical mean contribution of ΔP_R to ΔP increased from 42.5% to 61.8% following the insertion of the PC, accordingly, the mean contribution of ΔP_B decreased from 57.5% to 38.2%. These results indicate that a pressure guidewire increases the trans-stenosis pressure drop primarily via its role in augmenting viscous pressure loss. It is noted that

the integration of transient ΔP_L over a cardiac cycle should be theoretically close to zero. The extremely small values and relative contributions to ΔP of ΔP_L presented in FIGs. 6 (c) & (f) are a consequence of errors stemming from data regression and time integration of discrete data points (herein 100 data points) over a cardiac cycle, and hence do not deserve further analysis.

To explore the fluid dynamics mechanisms underlying the pressure guidewire-induced increase in viscous pressure loss (ΔP_R), we further analyzed the detailed flow field in an idealized LAD model with or without a PC (see FIG. 7). All the visualized data are those averaged over a cardiac cycle. The partial occupation of the vascular lumen by the PC led to marked changes in flow field. Specifically, the core of the trans-stenosis jet flow was split by the PC (FIGs. 7 (b) & (d)), leading to the formation of an additional boundary layer near the outer surface of the PC, which was more evidently identified if the velocity gradient, which is a major determinant of viscous loss, was calculated and visualized (FIG. 7 (e)). To more clearly illustrate the impact of the PC on flow velocity

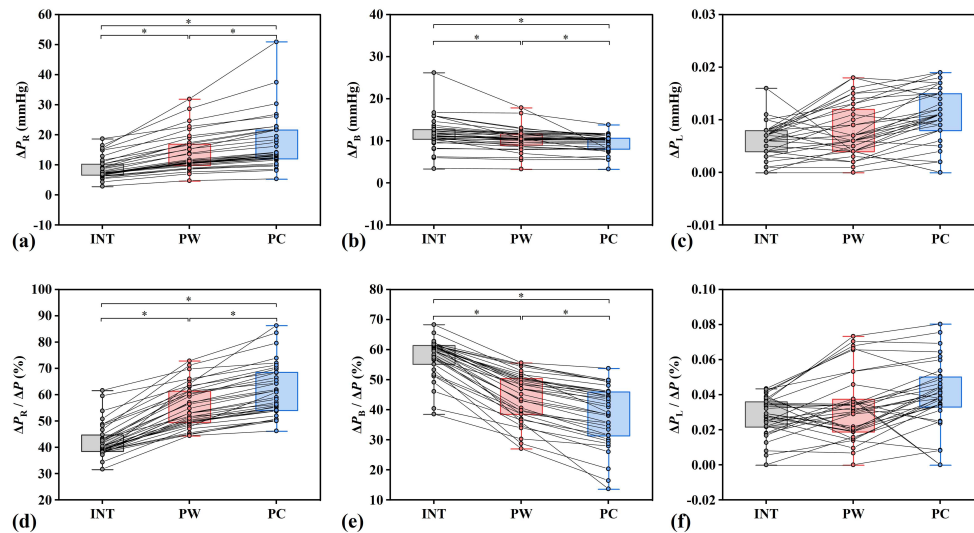


FIG. 6. Box plots of ΔP_R (a), ΔP_B (b), ΔP_L (c) decomposed from the computed total trans-stenosis pressure drops (ΔP) for all the LAD models without or with an inserted a pressure guidewire (PW or PC), and their percent proportions in ΔP (d-f). The scattered points represent individual data values, while the colored rectangles represent the lower and upper quartiles of each dataset with the error bars indicating the minimum and maximum values. All the inter-group comparisons are performed with paired t-test, with the stars (*) indicating a p value of <0.001 . See the caption of FIG. 4 for the interpretations of the abbreviations.

distribution, we plot the profiles of the flow velocity and velocity gradient at the stenosis throat (FIGs. 7 (f) & (g)). There were two separate velocity profiles and remarkably increased velocity gradient near the outer surface of the PC. In contrast, the contour maps of turbulent intensity showed that the presence of PC tended to reduce rather than enhance the intensity of turbulence (FIG. 7 (c)). These results indicate that the increased viscous pressure loss in the presence of a PC is attributable mainly to the flow boundary layer formed around the outer surface of the PC.

B. Influence of the characteristics of the LAD and stenosis on guidewire-induced changes in FFR

From this section, we put focus on investigating the impact of pressure guidewire on FFR. FIG. 8 shows the changes in FFRs in the idealized LAD models before and after the insertion of a PW or PC. The figure is divided into eight panels according to the variations in the morpho-geometrical parameters of the LAD or the severity, number, length, and morphological parameters of the stenosis. The subscripts 'INT', 'PC', and 'PW' indicate the FFRs computed under the intact (guidewire-absent) condition, and after the insertion of a PC or PW into the LAD, respectively. Insertion of a pressure guidewire led to a decrease of FFR in all the LAD models

due to the increased trans-stenosis pressure drop. The effects were more pronounced for the PC due to its larger diameter compared with the PW. The variations in LAD diameter, number of stenosis, and stenosis rate had the strongest influence on FFR and its change in response to the insertion of a PC or PW. Specifically, reducing LAD diameter and increasing stenosis rate or the number of stenosis resulted in an evident decrease in FFR and an augmentation of the guidewire-induced decrease in FFR. The influence of varying stenosis length was considerable, but not that strong as varying stenosis rate. Relatively, varying the curvature and tapering of the LAD and the axial and radial asymmetry of stenosis only had mild influence.

To investigate in quantitative detail the guidewire-induced changes in FFR, we plot the differences between FFR_{PW} or FFR_{PC} (guidewire-present FFR) and FFR_{INT} (guidewire-absent FFR) against FFR_{INT} in FIG. 9. Overall, the difference increased following the decrease in FFR_{INT} . In accordance with the results presented in FIG. 8, the difference was large in the cases with high stenosis rate, smaller vascular diameter, or multiple stenoses when FFR_{INT} was low. If the focus was put on the data in the diagnostic gray zone (i.e., $FFR_{INT} = 0.75-0.8$) where the stenosis rate is 55% and the diameter of LAD is fixed at 3.6mm (see the amplified subpanels in FIG. 9), it was observed that varying the length of stenosis had stronger influence on the guidewire-induced change in

This is the author's peer reviewed, accepted manuscript. However, the online version of record will be different from this version once it has been copyedited and typeset.

PLEASE CITE THIS ARTICLE AS DOI: 10.1063/1.50256403

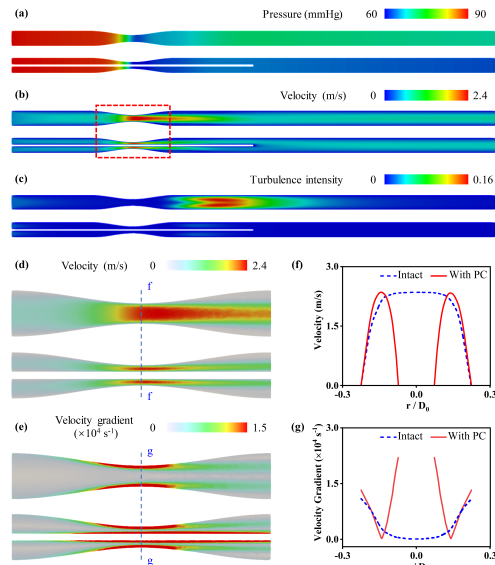


FIG. 7. Contour maps of blood pressure (a), flow velocity (b) and turbulence intensity (c) in the median longitudinal section of an idealized LAD model without or with an inserted PC, locally amplified contour maps of velocity (d) and velocity gradient (e) in the vicinity of the stenosis (surrounded by the rectangle in panel (b)), and profiles of velocity (f) and velocity gradient (g) in a cross-sectional cutting plane at the stenosis throat (indicated by the dash lines in panels (d) and (e)). It is noted that all the pictures are produced based on the time-averaged hemodynamic data over a cardiac cycle.

FFR than did varying other morphological parameters (e.g., eccentricity, curvature, or tapering) of stenosis or LAD.

In comparison with the idealized models, realistic LAD models have more complex morphological features. We compared the simulated results for the ten original realistic LAD models and the ten artificially straightened LAD models present with a PC. Straightening the LADs (i.e., removing vascular curvature) caused the flow rate to slightly increase ($\Delta Q=0.141\pm 0.038$ mL/s), leading to a mild decrease in FFR_{PC} ($\Delta FFR_{PC}=-0.009\pm 0.004$). Given the small values of ΔFFR_{PC} , the influence of vascular curvature on FFR can be considered negligible, which is consistent with the relevant finding on the idealized models. To explore the underlying hemodynamic mechanisms, the flow field in a selected realistic LAD model was analyzed (FIG. 10). The curvatures (denoted by the red arrows in FIG. 10 (b)) induced enhanced flow disturbance and asymmetry of cross-sectional velocity profile in the post-stenosis region (FIG. 10 (d)), which inherently increased the effective flow resistance along the LAD. In another word, artificially removing the curvatures could reduce the effective resistance of the LAD and increase the flow rate, thereby increasing the trans-stenosis pressure drop to reduce

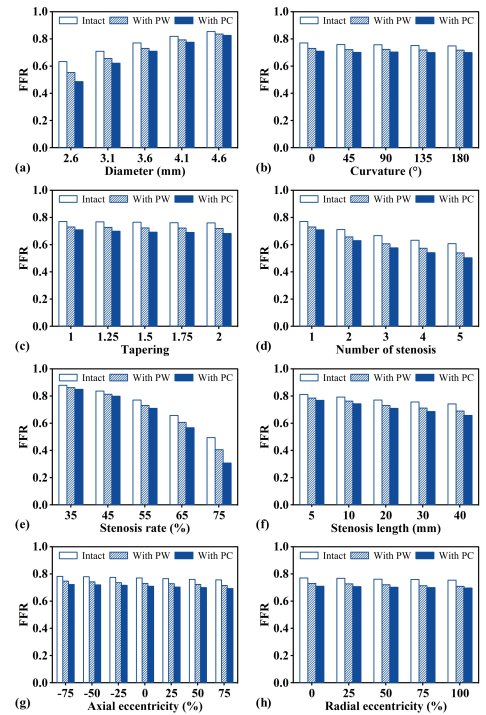


FIG. 8. Effects of varying the morpho-geometrical parameters of LAD (a-c), and the number, severity, length, and axial/radial eccentricity of stenosis (d-h) on the changes of FFR in response to the insertion of a PW or PC. It is noted that when one parameter is varied, other parameters are fixed at their default values in the baseline LAD model as described in the caption of TABLE I.

FFR (FIG. 10 (c)).

C. Relationship between intact and guidewire-present FFRs

The simulated FFRs for all the idealized and realistic LAD models present with a PW or PC are plotted against the intact (guidewire-absent) FFRs in FIG. 11 (a). Linear regression analysis revealed that the relationships of FFR_{PW} and FFR_{PC} with FFR_{INT} could be each represented by a linear function ($FFR_{PW}=1.189\times FFR_{INT}-0.184$, $FFR_{PC}=1.354\times FFR_{INT}-0.336$) with $r^2=0.99$. In particular, the linear relationship held true for both the idealized and realistic models (see the zoom-in subpanel in FIG. 11 (a)). From the mathematical expressions, the slope of the linear function was dependent on the diameter of the guidewire, which was smaller for FFR_{PW} while larger for FFR_{PC} .

To explore the underlying mechanisms, we constructed a simplified theoretical model. As shown in FIG. 11 (b), the

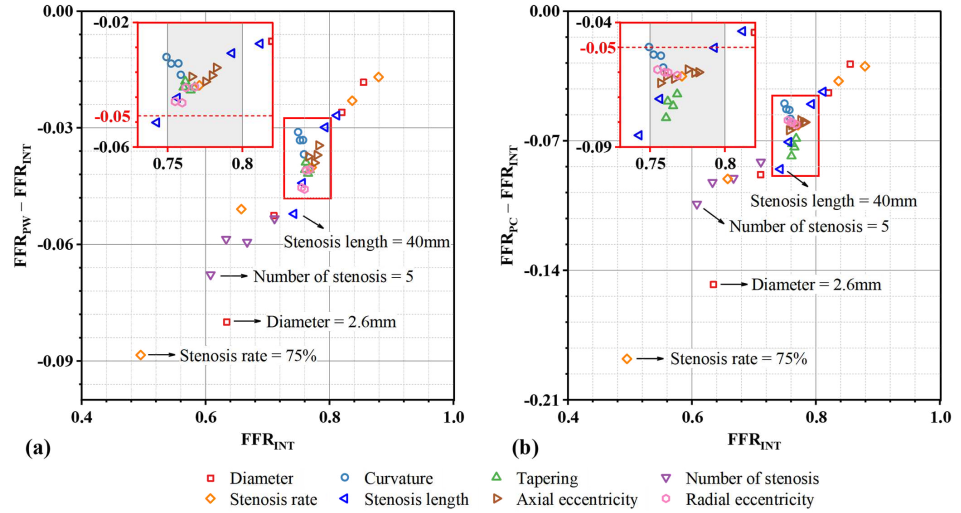


FIG. 9. Scatter plots of the differences between FFR_{PW} (a)/ FFR_{PC} (b) and FFR_{INT} computed for all the idealized LAD models. Some data points are labeled with the corresponding morpho-geometrical parameters. In each panel, the data points in the gray zone of FFR (0.75-0.8) are highlighted by a zoom-in subpanel to more clearly show how the variations of morpho-geometrical parameters (note that herein stenosis rate is fixed at 55%) affect the differences between guidewire-present and guidewire-absent FFRs. Subscripts: INT, intact condition (absence of a pressure guidewire); PW, presence of a pressure wire; PC, presence of a pressure catheter.

LAD branch of the coronary circulation was divided into two portions, one represents the proximal portion of the LAD (containing the stenosis) and the other one represents the vessels distal to the stenosis, with their effective resistances being denoted by R_{INT} and R_D , respectively. The flow rate and trans-stenosis pressure drop were denoted by Q_{INT} and ΔP_{INT} , respectively. After the insertion of a pressure guidewire, the upstream aortic pressure (P_A), distal venous pressure (P_V), and R_D were assumed to remain unchanged, whereas R_{INT} , Q_{INT} , and ΔP_{INT} changed into R_G , Q_G , and ΔP_G , respectively. According to the definition of FFR, we can deduce the following equation.

$$\frac{\Delta P_G}{\Delta P_{INT}} = \frac{P_A \times (1 - FFR_G)}{P_A \times (1 - FFR_{INT})}, \quad (3)$$

Given $\Delta P_G/\Delta P_{INT}$, FFR_G can be expressed as a function of FFR_{INT} as

$$FFR_G = \frac{\Delta P_G}{\Delta P_{INT}} \times FFR_{INT} + \left(1 - \frac{\Delta P_G}{\Delta P_{INT}}\right), \quad (4)$$

$\Delta P_G/\Delta P_{INT}$ can be rewritten as a function of the resistances

according to the fluid mechanics theory as

$$\begin{aligned} \frac{\Delta P_G}{\Delta P_{INT}} &= \frac{Q_G \times R_G}{Q_{INT} \times R_{INT}} \\ &= \frac{(P_A - P_V)/(R_G + R_D) \times R_G}{(P_A - P_V)/(R_{INT} + R_D) \times R_{INT}}, \quad (5) \\ &= \frac{(R_{INT} + R_D) \times R_G}{(R_G + R_D) \times R_{INT}} \end{aligned}$$

By further reorganizing Eq. (5), we obtained

$$\frac{\Delta P_G}{\Delta P_{INT}} = \frac{R_{INT}/R_D + 1}{R_{INT}/R_D + R_{INT}/R_G}. \quad (6)$$

FIG. 11 (c) shows the surface plot of $\Delta P_G/\Delta P_{INT}$ when R_{INT}/R_D and R_{INT}/R_G are each varied over a large range. It is observed that when $\Delta P_G/\Delta P_{INT}$ is below 2 and R_{INT}/R_G is constant the variations of $\Delta P_G/\Delta P_{INT}$ with respect to R_{INT}/R_D are minor. The simulated values of $\Delta P_G/\Delta P_{INT}$ for the forty-five LAD models were all lower than 2. Although R_{INT}/R_D exhibited large variations (caused mainly by the differential stenosis rates), the changes of $\Delta P_G/\Delta P_{INT}$ were small due to the small variations of R_{INT}/R_G . In addition, because R_{INT}/R_G computed for the PW and PC differed considerably, the corresponding $\Delta P_G/\Delta P_{INT}$ distributed in different zones on the surface. The small changes in $\Delta P_G/\Delta P_{INT}$ means that the slope and intercept in Eq.(4) are close to constant values, which justifies the existence of an approximately linear relationship between FFR_G and FFR_{INT} . In addition, the sum

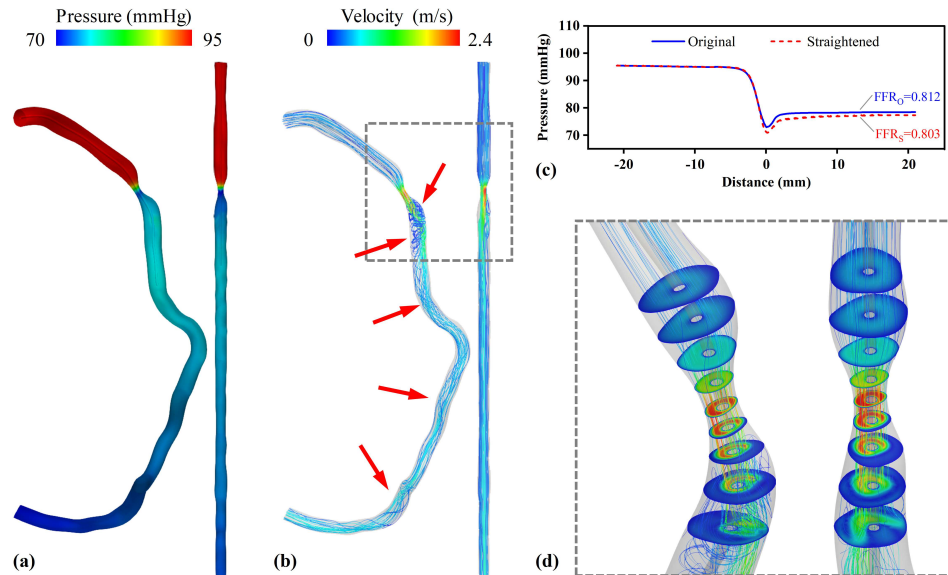


FIG. 10. Contour maps of the time-averaged blood pressure (a), and flow streamlines (b) in a realistic LAD model embedded with a PC before and after the straightening treatment, changes in the cross-sectionally mean blood pressure along the LAD and the corresponding FFRs (c), and flow streamlines and cross-sectional velocity contours in the vicinity of the stenosis (denoted by the rectangle in panel (b)) (d). It is noted that all the pictures are produced based on the time-averaged hemodynamic data over a cardiac cycle.

of the slope and intercept is theoretically equal to 1, which was confirmed by the regressed linear functions for FFR_{PW} and FFR_{PC} whose slope and intercept add up to be 1.005 and 1.018, respectively.

IV. DISCUSSION

A 0-3D multiscale model was developed to provide a tool for quantifying the influence of pressure guidewire on coronary hemodynamics and FFR. In comparison with the models employed in previous studies¹⁶⁻¹⁸, a major advantage of our model lies in that it can account for, in an automatic and physiologically reasonable way, the hemodynamic changes induced by the insertion of a pressure guidewire into the coronary artery. Model-based numerical studies demonstrated the reduced flow rate, increased trans-stenosis pressure drop, and decreased FFR following the insertion of a pressure guidewire into the coronary artery, and elucidated that the increased viscous pressure loss along the outer surface of the pressure guidewire is a major mechanism underlying the observed hemodynamic changes. More importantly, the numerical experiments on forty-five LAD models demonstrated that FFRs computed in the presence of a pressure guidewire were strongly correlated with the guidewire-absent FFRs, and their relationship could be well depicted with a linear function.

Some previous studies have reported data showing strong linear correlations between guidewire-present FFRs and guidewire-absent FFRs^{12,17,35}, however, they did not investigate in detail how the correlations would be affected by multiple factors and explore the underlying mechanisms. In this study, we firstly confirmed through model-based numerical experiments that the guidewire-present FFRs can be expressed as a linear function of the guidewire-absent FFRs despite the variations in stenosis rate and morpho-geometrical characteristics of the LAD, and further developed a theoretical model to elucidate why the linear relationship exists. The theoretical model revealed that the insensitivity of the ratio of the guidewire-present trans-stenosis pressure to the guide-absent one ($\Delta P_G / \Delta P_{INT}$) to the variations of $\Delta R_{INT} / \Delta R_D$ (ratio of the effective resistance of the stenosed LAD to the distal resistance) and the relative small variations of $\Delta R_{INT} / \Delta R_G$ (ratio of the effective resistances of the stenosed LAD before and after guidewire insertion) together determine the existence of a linear relationship between guidewire-present and guidewire-absent FFRs.

The findings may have important clinical implications. For instance, when the predicted FFRs by models without a pressure guidewire are to be used to classify coronary artery stenoses based on the threshold of FFR (e.g., 0.75/0.8) established based on invasively measured data with pressure wires^{36,37}, the threshold should be adjusted to 0.786/0.828.

This is the author's peer reviewed, accepted manuscript. However, the online version of record will be different from this version once it has been copyedited and typeset.

PLEASE CITE THIS ARTICLE AS DOI: 10.1063/1.50256403

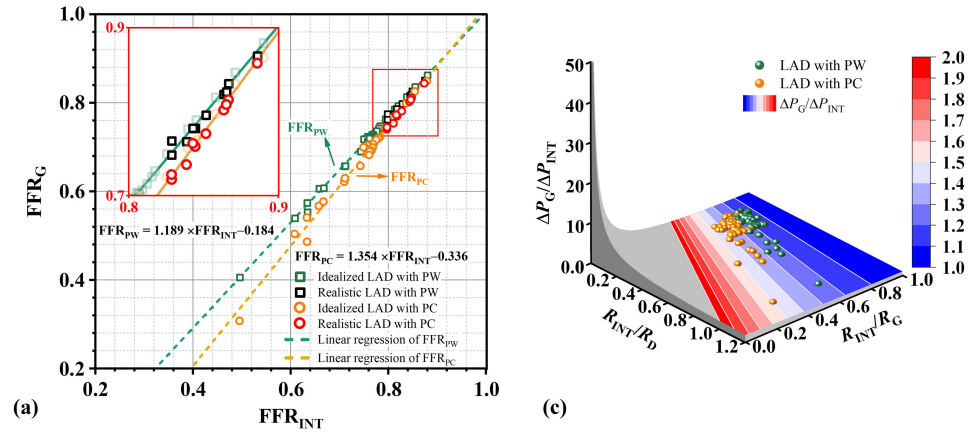


FIG. 11. Scatter plots of guidewire-present FFRs (FFR_G) against intact guidewire-free FFRs (FFR_{INT}) computed for all the LAD models (including thirty-five idealized and ten realistic models) (a), a simplified theoretical model describing the hemodynamics in a LAD branch with or without a pressure guidewire (b), and surface plot of $\Delta P_G / \Delta P_{INT}$ as a function of R_{INT}/R_G and R_{INT}/R_D superimposed with the scatter plots of the computed $\Delta P_G / \Delta P_{INT}$ for all the LAD models involved in the study (c). In panel (a), the data are analyzed with linear regression, yielding two linear functions depicting the relationships between FFR_{PW} and FFR_{INT} and between FFR_{PC} and FFR_{INT} , respectively. Abbreviations: P_A , aortic pressure; P_V , venous pressure; ΔP , trans-stenosis pressure drop; Q , blood flow rate; R , effective resistance; INT, intact guidewire-absent condition; G, present with a guidewire; D, distal.

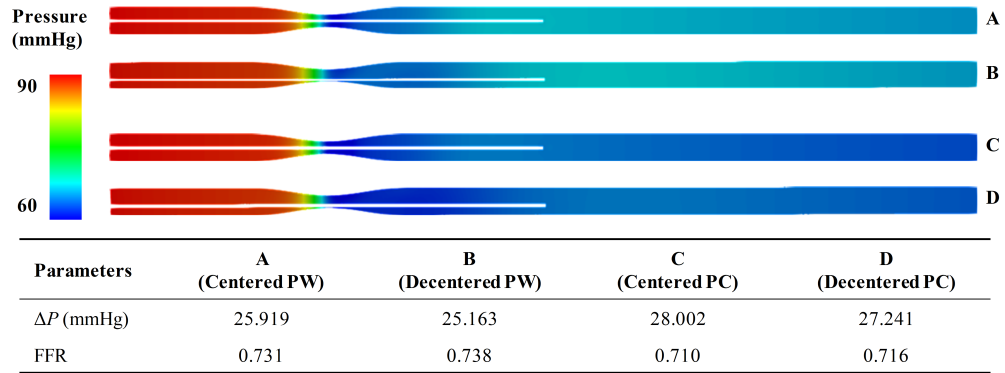


FIG. 12. Contour maps of the time-averaged blood pressure in a LAD model embedded with a pressure guidewire (PW or PC) positioned centrally (along vascular centerline) or eccentrically (close to the lumen surface) and the computed trans-stenosis pressure drop (ΔP) and FFR.

On the other hand, the linear relationship between guidewire-present FFRs and guidewire-absent FFRs may also be utilized to convert invasively measured FFRs into the guidewire-absent ones so as to better assess the functional impact of coronary artery stenosis under intact physiological conditions. If the influence of a pressure guidewire on FFR in a specific coronary artery is of interest, high stenosis rate, small vascular diameter and coexistence of multiple serial stenoses should be the factors of concern since they significantly augment the difference between guidewire-present FFR and guidewire-absent FFR. For moderate stenoses whose FFRs are usually in the diagnostic gray zone (i.e., 0.75-0.8), the length of stenosis is also an important factor deserving consideration.

V. LIMITATIONS

Our study is subjected to certain limitations. Firstly, the study is theoretical, although realistic LAD models were involved. Comparing the simulated FFRs for realistic LADs against in-vivo measurements would better confirm the validity of our modeling method, which however requires the calibration of the parameters in the 0D model based on patient-specific clinical data that were not available in the present study. We are collecting clinical data to address this limitation. Secondly, we placed the pressure guidewire along the vascular centerline, although in reality the position of pressure guidewire may deviate from the centerline due to the influence of complex vascular morphology and hemodynamic force. To address this issue, we performed numerical experiments on a LAD model where the position of PW or PC was moved toward the vascular lumen surface. The results showed that changing the position of guidewire induced little changes (<1%) in simulated FFR (see FIG. 12). Thirdly, the blood was modeled as a Newtonian fluid in the present study, although the rheological properties of blood are inherently non-Newtonian, usually exhibiting a shear-thinning behavior characterized by the decrease of viscosity with the increase in shear rate of flow. Our numerical experiments conducted on a randomly selected LAD model showed that the shear rate-dependent variations of blood viscosity were small owing to the overall high level of shear rate, and that employing a non-Newtonian model to account for the shear-thinning effect of blood (herein the Carreau's model) did not considerably alter the results of numerical simulations, causing the computed FFRs to differ only slightly (about 1%) from those by the Newtonian model. Given the small differences, the Newtonian fluid assumption adopted in our study should not be a limitation significantly compromising the validity of the presented findings. Fourthly, the wall of coronary artery was assumed to be rigid, which is inconsistent with the inherent mechanical properties of vascular wall. Since the study is focused on FFR which is calculated based on the mean blood pressures during a cardiac cycle and the radial deformation of coronary artery is small³⁸, the assumption may not significantly compromise the validity of the numerical results. Fifthly, we fixed the vascular resistance distal to the LAD (i.e., R_D in Eqs. (5) and (6)) in all the simulations. However, R_D should differ among

patients, and may increase over the assigned baseline value in patients with microvascular dysfunction. Fortunately, our theoretical study demonstrated that varying the ratio of R_{INT} to R_D has small influence on $\Delta P_G/\Delta P_{INT}$, and hence the variations of R_D in physiological ranges would not considerably compromise the validity of the linear relationships between guidewire-present and guidewire-absent FFRs established in the present study.

VI. CONCLUSIONS

In this study, a 0-3D geometrical multiscale modeling method was employed to quantitatively address the influence of the intravascular placement of a pressure guidewire on the hemodynamic characteristics and FFR in the LAD. The study firstly revealed that a pressure guidewire enlarges the transstenosis pressure drop and reduces FFR mainly via its role in augmenting viscous pressure loss. The diameter of the LAD, the severity and number of stenosis, and the diameter of pressure guidewire were found to be the major factors affecting the degree of FFR decrease following the insertion of a pressure guidewire. Statistical analysis on the numerical results further indicated the existence of a linear relationship between guidewire-present FFRs and guidewire-absent FFRs despite the variations in the morpho-geometrical characteristics of the LAD or the severity of stenosis, with the slope and intercept of the linear function being determined primarily by the diameter of the guidewire. These findings not only enable a better understanding of the mechanisms underlying the pressure guidewire-induced hemodynamic changes in the coronary artery, but also provide theoretical references for explaining or correcting the discrepancies between FFRs predicted by guidewire-absent CFD models and invasively measured FFRs.

ACKNOWLEDGMENTS

The research was supported by the joint NSFC-RSF project (the National Natural Science Foundation of China, grant No. 12061131015; Russian Science Foundation, grant No. 21-41-00029).

AUTHOR DECLARATIONS

Conflict of Interest

The authors have no conflicts to disclose.

Ethical Approval

The use of medical images in this study was approved by the Ethics Committee of the Shanghai Ninth People's Hospital (approval No. SH9H2019T1604).

This is the author's peer reviewed, accepted manuscript. However, the online version of record will be different from this version once it has been copyedited and typeset.

PLEASE CITE THIS ARTICLE AS DOI: 10.1063/1.50256403

Author Contributions

Xuanyu Li: Writing – review & editing, Writing – original draft, Visualization, Validation, Software, Methodology, Investigation, Formal analysis, Data curation, Conceptualization. **Zhi Zhang:** Writing – review & editing, Resources, Investigation, Formal analysis, Conceptualization. **Sergey Simakov:** Writing – review & editing, Methodology, Investigation, Funding acquisition, Conceptualization. **Timur Gamilov:** Writing – review & editing, Resources, Methodology, Investigation, Validation. **Yuri Vassilevski:** Writing – review & editing, Methodology, Investigation, Conceptualization. **Yue Wang:** Writing – review & editing, Resources, Investigation. **Fuyou Liang:** Writing – review & editing, Validation, Supervision, Resources, Project administration, Methodology, Investigation, Funding acquisition, Conceptualization.

DATA AVAILABILITY STATEMENT

The data that support the findings of this study are available from the corresponding author upon reasonable request.

APPENDIX

This is the author's peer reviewed, accepted manuscript. However, the online version of record will be different from this version once it has been copyedited and typeset.

PLEASE CITE THIS ARTICLE AS DOI: 10.1063/1.50256403

TABLE III. Assigned parameter values for the OD model under the hyperemic condition (see Fig.1 for the distribution of the parameters in the model). Units of parameters: pressure (P), mmHg; elastance (E), mmHg·ml⁻¹; viscoelasticity coefficient (S), mmHg·s·ml⁻¹; resistance (R), mmHg·s·ml⁻¹; inertance (L), mmHg·s²·ml⁻¹; compliance (C), ml/mmHg; Bernoulli's resistance (B), mmHg·s²·ml⁻².

Heart					
$E_{ra}=0.13$	$E_{rv}=0.48$	$E_{la}=0.25$	$E_{lv}=3.44$	$S_{ra}=P_{ra} \times 5E-4$	$S_{rv}=P_{rv} \times 5E-4$
$S_{la}=P_{la} \times 5E-4$	$S_{lv}=P_{lv} \times 5E-4$	$P_{pc}=3.0$			
Cardiac valves					
$L_{rv}=5E-4$	$B_{rv}=1E-5$	$R_{rv}=1E-3$	$L_{pv}=5E-4$	$B_{pv}=1.5E-5$	$R_{pv}=1.5E-3$
$L_{mv}=5E-4$	$B_{mv}=1E-5$	$R_{mv}=1E-3$	$L_{av}=5E-4$	$B_{av}=1.5E-5$	$R_{av}=1.5E-3$
Pulmonary circulation					
$L_{pua}=5E-4$	$R_{pua}=0.035$	$C_{pua}=2.45$	$L_{puc}=2E-4$	$R_{puc}=0.0259$	$C_{puc}=19.89$
$L_{puv}=3E-4$	$R_{puv}=0.0152$	$C_{puv}=8.26$	$P_{it}=-3.5$		
Systemic circulation					
Aorta	$L_{ao,l}=6E-3$	$R_{ao,l}=0.026$	$C_{ao}=1.13$		
Lower body	$L_{art,l}=5E-3$	$R_{art,l}=0.77$	$C_{art,l}=0.56$	$L_{cap,l}=5E-4$	$R_{cap,l}=0.18$
	$C_{cap,l}=0.26$	$L_{ven,l}=1E-3$	$R_{ven,l}=0.037$	$C_{ven,l}=93.2$	
Upper body	$L_{art,u}=5E-3$	$R_{art,u}=1.806$	$C_{art,u}=0.076$	$L_{cap,u}=5E-4$	$R_{cap,u}=0.43$
	$C_{cap,u}=0.036$	$L_{ven,u}=1E-3$	$R_{ven,u}=0.086$	$C_{ven,u}=12.7$	
Vena cava	$L_{vc}=5E-4$	$R_{vc}=4.3E-3$	$C_{vc}=19.03$		
Large coronary arteries					
$L_{lm}=4.7E-4$	$R_{lm}=0.036$	$C_{lm}=7.8E-4$	$L_{lcx}=0.307$	$R_{lcx}=8.3$	$C_{lcx}=1.9E-3$
$L_{lad,p}=3E-3$	$R_{lad,p}=0.03$	$C_{lad,p}=8E-4$	$L_{lad,3d}=3E-3$	$C_{lad,3d}=8E-4$	$L_{lad,d}=0.29$
$R_{lad,d}=6.34$	$C_{lad,d}=1.9E-3$	$L_{rca}=0.307$	$R_{rca}=7.245$	$C_{rca}=1.6E-3$	
Intramyocardial vessels					
	$R_c=9.8$	$L_1=0.117$	$R_1=13.65$	$C_1=9.98E-4$	$L_2=0.059$
LAD	$R_2=6.825$	$C_2=2.7E-3$	$L_3=0.02$	$R_3=2.275$	$C_3=3.3E-3$
	$L_v=0.767$	$R_v=2.45$	$C_v=3.5E-3$		
	$R_c=9.296$	$L_1=0.117$	$R_1=12.948$	$C_1=9.98E-4$	$L_2=0.059$
LCX	$R_2=6.474$	$C_2=2.7E-3$	$L_3=0.02$	$R_3=2.158$	$C_3=3.3E-3$
	$L_v=0.707$	$R_v=2.324$	$C_v=3.5E-3$		
	$R_c=9.976$	$L_1=0.117$	$R_1=13.896$	$C_1=9.98E-4$	$L_2=0.059$
RCA	$R_2=6.948$	$C_2=2.7E-3$	$L_3=0.02$	$R_3=2.316$	$C_3=3.3E-3$
	$L_v=0.707$	$R_v=2.494$	$C_v=3.5E-3$		
$P_{im,epi}=P_{lv} \times 0.1$		$P_{im,mid}=P_{lv} \times 0.5$		$P_{im,endo}=P_{lv} \times 0.9$	

REFERENCES

- ¹S. Bangalore, E. R. Bates, T. M. Beckie, J. M. Bischoff, J. A. Bittl, M. G. Cohen, J. M. DiMaio, C. W. Don, S. E. Fremes, M. F. Gaudino, *et al.*, "2021 acc/aha/scat guideline for coronary artery revascularization," *Journal of the American College of Cardiology* **79**, E21–E129 (2022).
- ²A. P. Kerkar, J. H. Juratli, A. A. Kumar, T. A. McLaren, and N. R. Sutton, "Best practices for physiologic assessment of coronary stenosis," *Current Treatment Options in Cardiovascular Medicine* **25**, 159–174 (2023).
- ³K. L. Gould, R. L. Kirkeeide, and M. Buchi, "Coronary flow reserve as a physiologic measure of stenosis severity," *Journal of the American College of Cardiology* **15**, 459–474 (1990).
- ⁴N. H. Pijls, B. de Bruyne, K. Peels, P. H. van der Voort, H. J. Bonnier, J. Bartunek, and J. J. Koolen, "Measurement of fractional flow reserve to assess the functional severity of coronary-artery stenoses," *New England Journal of Medicine* **334**, 1703–1708 (1996).
- ⁵Y. Matsuo, Y. Shiono, K. Kashiyama, Y. Ino, T. Nishi, K. Terada, H. Emori, D. Higashioka, Y. Katayama, A. K. Mahfouz, *et al.*, "Extent of the difference between microcatheter and pressure wire-derived fractional flow reserve and its relation to optical coherence tomography-derived parameters," *IJC Heart & Vascular* **27**, 100500 (2020).
- ⁶C. A. Taylor, T. A. Fonte, and J. K. Min, "Computational fluid dynamics applied to cardiac computed tomography for noninvasive quantification of fractional flow reserve: scientific basis," *Journal of the American College of Cardiology* **61**, 2233–2241 (2013).
- ⁷J. K. Min, C. A. Taylor, S. Achenbach, B. K. Koo, J. Leipsic, B. L. Nørgaard, N. J. Pijls, and B. De Bruyne, "Noninvasive fractional flow reserve derived from coronary ct angiography: clinical data and scientific principles," *Cardiovascular Imaging* **8**, 1209–1222 (2015).
- ⁸C. X. Tang, C. Y. Liu, M. J. Lu, U. J. Schoepf, C. Tesche, R. R. Bayer, H. T. Hudson Jr, X. L. Zhang, J. H. Li, Y. N. Wang, *et al.*, "Ct ffr for ischemia-specific cad with a new computational fluid dynamics algorithm: a chinese multicenter study," *Cardiovascular Imaging* **13**, 980–990 (2020).
- ⁹B. Zhuang, S. Wang, S. Zhao, and M. Lu, "Computed tomography angiography-derived fractional flow reserve (ct-ffr) for the detection of myocardial ischemia with invasive fractional flow reserve as reference: systematic review and meta-analysis," *European radiology* **30**, 712–725 (2020).
- ¹⁰S. Tu, J. Westra, J. Adedj, D. Ding, F. Liang, B. Xu, N. R. Holm, J. H. Reiber, and W. Wijns, "Fractional flow reserve in clinical practice: from wire-based invasive measurement to image-based computation," *European Heart Journal* **41**, 3271–3279 (2020).
- ¹¹J. Peper, M. L. Bots, T. Leiner, and M. J. Swaans, "Non-invasive angiographic-based fractional flow reserve: Technical development, clinical implications, and future perspectives," *Current medical science* **43**, 423–433 (2023).
- ¹²K. D. Ashtekar, L. H. Back, S. F. Khoury, and R. K. Banerjee, "In vitro quantification of guidewire flow-obstruction effect in model coronary stenoses for interventional diagnostic procedure," *Journal of Medical Devices* **1**, 185–196 (2007).
- ¹³R. K. Banerjee, S. V. Peelukhana, and I. Goswami, "Influence of newly designed monorail pressure sensor catheter on coronary diagnostic parameters: An in vitro study," *Journal of Biomechanics* **47**, 617–624 (2014).
- ¹⁴E. Rajabi-Jaghargh, K. K. Kolli, L. H. Back, and R. K. Banerjee, "Effect of guidewire on contribution of loss due to momentum change and viscous loss to the translesional pressure drop across coronary artery stenosis: An analytical approach," *Biomedical engineering online* **10**, 1–22 (2011).
- ¹⁵D.-Y. Kang, J.-M. Ahn, Y. W. Kim, J. Y. Moon, J. S. Lee, B.-K. Koo, P. H. Lee, D.-W. Park, S.-J. Kang, S.-W. Lee, *et al.*, "Impact of coronary lesion geometry on fractional flow reserve: data from interventional cardiology research in-cooperation society-fractional flow reserve and intravascular ultrasound registry," *Circulation: Cardiovascular Imaging* **11**, e007087 (2018).
- ¹⁶J. Yi, F.-B. Tian, A. Simmons, and T. Barber, "A computational analysis of the influence of a pressure wire in evaluating coronary stenosis," *Fluids* **6**, 165 (2021).
- ¹⁷A. Lucca, L. Fracarrolo, F. E. Fossan, A. T. Bråten, S. Pozzi, C. Vergara, and L. O. Müller, "Impact of pressure guidewire on model-based ffr prediction," *Cardiovascular Engineering and Technology* , 1–13 (2024).
- ¹⁸J. Wang, Z. Hao, B. Yin, W. Tan, and C. Zhu, "Effect of guidewire on the accuracy of trans-stenotic pressure measurement—a computational study," *Physics of Fluids* **36** (2024).
- ¹⁹A. S. Roy, L. H. Back, and R. K. Banerjee, "Guidewire flow obstruction effect on pressure drop-flow relationship in moderate coronary artery stenosis," *Journal of biomechanics* **39**, 853–864 (2006).
- ²⁰D. Tang, C. Yang, S. Kobayashi, J. Zheng, and R. P. Vito, "Effect of stenosis asymmetry on blood flow and artery compression: a three-dimensional fluid-structure interaction model," *Annals of biomedical engineering* **31**, 1182–1193 (2003).
- ²¹J. Adedj, B. De Bruyne, V. Floré, G. Di Gioia, A. Ferrara, M. Pellicano, G. G. Toth, J. Bartunek, M. Vanderheyden, G. R. Heyndrickx, *et al.*, "Significance of intermediate values of fractional flow reserve in patients with coronary artery disease," *Circulation* **133**, 502–508 (2016).
- ²²M. Solecki, M. Kruk, M. Demkow, U. J. Schoepf, M. A. Reynolds, Ł. Wardziak, Z. Dzielińska, M. Śpiewak, B. Miłośz-Wieczorek, Ł. Małek, *et al.*, "What is the optimal anatomic location for coronary artery pressure measurement at ct-derived ffr?" *Journal of Cardiovascular Computed Tomography* **11**, 397–403 (2017).
- ²³X. Li, S. Simakov, Y. Liu, T. Liu, Y. Wang, and F. Liang, "The influence of aortic valve disease on coronary hemodynamics: A computational model-based study," *Bioengineering* **10**, 709 (2023).
- ²⁴F. Liang, H. Senzaki, C. Kurishima, K. Sughimoto, R. Inuzuka, and H. Liu, "Hemodynamic performance of the fontan circulation compared with a normal biventricular circulation: a computational model study," *American Journal of Physiology-Heart and Circulatory Physiology* **307**, H1056–H1072 (2014).
- ²⁵X. Ge, Y. Liu, Z. Yin, S. Tu, Y. Fan, Y. Vassilevski, S. Simakov, and F. Liang, "Comparison of instantaneous wave-free ratio (iwr) and fractional flow reserve (ffr) with respect to their sensitivities to cardiovascular factors: a computational model-based study," *Journal of interventional cardiology* **2020**, 4094121 (2020).
- ²⁶X. Ge, Y. Liu, S. Tu, S. Simakov, Y. Vassilevski, and F. Liang, "Model-based analysis of the sensitivities and diagnostic implications of ffr and cfr under various pathological conditions," *International journal for numerical methods in biomedical engineering* **37**, e3257 (2021).
- ²⁷A. Nitenberg, J.-M. Foul, I. Antony, F. Blanchet, and M. Rahali, "Coronary flow and resistance reserve in patients with chronic aortic regurgitation, angina pectoris and normal coronary arteries," *Journal of the American College of Cardiology* **11**, 478–486 (1988).
- ²⁸P. Meimoun, A. L. Germain, F. Elmkies, T. Benali, J. Boulanger, C. Espagnol, J. Clerc, H. Zemir, A. Luyckx-Bore, and C. Tribouilloy, "Factors associated with noninvasive coronary flow reserve in severe aortic stenosis," *Journal of the American Society of Echocardiography* **25**, 835–841 (2012).
- ²⁹F. Liang, S. Takagi, R. Himeno, and H. Liu, "Multi-scale modeling of the human cardiovascular system with applications to aortic valvular and arterial stenoses," *Medical & biological engineering & computing* **47**, 743–755 (2009).
- ³⁰N. Freidoonimehr, M. Arjomandi, N. Sedaghatizadeh, R. Chin, and A. Zander, "Transitional turbulent flow in a stenosed coronary artery with a physiological pulsatile flow," *International Journal for Numerical Methods in Biomedical Engineering* **36**, e3347 (2020).
- ³¹R. K. Banerjee, K. D. Ashtekar, T. A. Helmy, M. A. Effat, L. H. Back, and S. F. Khoury, "Hemodynamic diagnostics of epicardial coronary stenoses: in-vitro experimental and computational study," *Biomedical engineering online* **7**, 1–22 (2008).
- ³²J. Ryval, A. Straatman, and D. Steinman, "Two-equation turbulence modeling of pulsatile flow in a stenosed tube," *J. Biomech. Eng.* **126**, 625–635 (2004).
- ³³D. F. Young and F. Y. Tsai, "Flow characteristics in models of arterial stenoses—i. steady flow," *Journal of biomechanics* **6**, 395–410 (1973).
- ³⁴D. F. Young and F. Y. Tsai, "Flow characteristics in models of arterial stenoses—ii. unsteady flow," *Journal of biomechanics* **6**, 547–559 (1973).
- ³⁵A. S. Roy, R. K. Banerjee, L. H. Back, M. R. Back, S. Khoury, and R. W. Millard, "Delineating the guide-wire flow obstruction effect in assessment of fractional flow reserve and coronary flow reserve measurements," *American Journal of Physiology-Heart and Circulatory Physiology* **289**, H392–H397 (2005).
- ³⁶B. De Bruyne and J. Sarma, "Fractional flow reserve: a review," *Heart* **94**, 949–959 (2008).

This is the author's peer reviewed, accepted manuscript. However, the online version of record will be different from this version once it has been copyedited and typeset.

PLEASE CITE THIS ARTICLE AS DOI: 10.1063/1.50256403

³⁷S. Morteza, A. M. Mohammad, A. P. Saeed, K. Isa, and N. Mohamadreza, "The role of ffr in clinical decision making in patients with moderate coronary lesions: a pilot study," *Acta Bio Medica: Atenei Parmensis* **89**, 378 (2018).

³⁸R. Torii, N. B. Wood, N. Hadjiloizou, A. W. Dowsey, A. R. Wright, A. D. Hughes, J. Davies, D. P. Francis, J. Mayet, G.-Z. Yang, *et al.*, "Fluid-structure interaction analysis of a patient-specific right coronary artery with physiological velocity and pressure waveforms," *Communications in numerical methods in engineering* **25**, 565–580 (2009).